Paleoceanography and Paleoclimatology

RESEARCH ARTICLE
10.1029/2021PA004349

A Deep-Time Dating Tool for Paleo-Applications Utilizing Obliquity and Precession Cycles: The Role of Dynamical Ellipticity and Tidal Dissipation

Richard E. Zeebe[1] **and Lucas J. Lourens**[2]

[1]School of Ocean and Earth Science and Technology, University of Hawaii at Manoa, Honolulu, HI, USA, [2]Department of Earth Sciences, Faculty of Geosciences, Utrecht University, Utrecht, The Netherlands

Key Points:

- We present an accurate dating method for paleoceanographic and paleoclimatologic deep-time records using obliquity and precession cycles
- We provide absolute geologic ages (early Eocene) with estimated uncertainty smaller than or equal to uncertainties from radiometric dating
- We include a quickstart guide to our approach and make our code and pre-computed solutions freely available to users

Correspondence to:
R. E. Zeebe,
zeebe@soest.hawaii.edu

Citation:
Zeebe, R. E., & Lourens, L. J. (2022). A deep-time dating tool for paleo-applications utilizing obliquity and precession cycles: The role of dynamical ellipticity and tidal dissipation. *Paleoceanography and Paleoclimatology*, *37*, e2021PA004349. https://doi.org/10.1029/2021PA004349

Received 22 AUG 2021
Accepted 7 JAN 2022

Abstract Pre-Pleistocene age models used in paleoceanography and paleoclimatology often rely on the imprint of astronomically calculated cycles of eccentricity and other solar system frequencies in sedimentary records (e.g., 405, 173, and ~100 kyr). However, use of obliquity and precession cycles (at present ~41 and ~20 kyr) remains challenging for these periods, mostly due to past changes in Earth's dynamical ellipticity (E_d, gravitational shape) and tidal dissipation (T_d, slowdown of Earth's rotation), which affect the astronomical calculations. Here, we present a dating method for deep-time records by integrating E_d and T_d into astrochronology. The key to our approach is the combination of constraints on T_d (and thus indirectly on E_d) with age model optimization based on solar system frequencies, plus tuning to obliquity/precession frequencies, while varying T_d and E_d. Importantly, we target deep-time intervals where T_d shows significant effects but high-quality sedimentary records are available (early Cenozoic). We include a quickstart guide to our approach and make our code and pre-computed solutions freely available to users. To demonstrate the practical utility of our approach, we apply our tool to two case studies using deep-sea records from the early and middle Eocene. Our results confirm very accurate chronologies of sedimentary records from the early Eocene (~56–54 Ma) but suggest significant improvement for the middle Eocene (~40–39 Ma). For the early Eocene, our method provides absolute geologic ages with an estimated uncertainty of ±20–40 kyr, which is smaller than or equal to typical uncertainties from recent radiometric $^{40}Ar/^{39}Ar$ dating.

1. Introduction

In 1754, Immanuel Kant wrote: "Accordingly, there can be no further doubt that the perpetual motion of the world ocean from east to west, as it is a real and considerable force, always contributes somewhat to the diminution of the axial rotation of the Earth, the results of which must become infallibly perceptible over long periods" (Kant, 1754). While Kant's remarkable insight into the workings of tidal dissipation is widely accepted today, its precise action over long periods is still uncertain, including the geologic past. In fact, this uncertainty presents one of the main challenges to calibrating the astronomical timescale (ATS) in deep-time based on astronomical periods associated with Earth's spin axis, that is, obliquity (tilt) and precession periods (caused by nutation and rotation of the spin axis itself). For instance, a 20% change in the tidal dissipation rate causes a phase shift by almost 180° in the numerical solution for obliquity over 15 Myr (see Figure 1). Thus, constraints on, and integration of, tidal dissipation (and dynamical ellipticity) into astrochronology provides a significant advance in dating of deep-time records. Note that for practical reasons the present study focuses on the early Cenozoic where tidal dissipation shows significant effects and high-quality records are available, but our approach can be applied to other timescales. One possible limitation for deep-time records is the requirement for a valid, stable, and well-expressed 405-kyr eccentricity cycle, as well as a robust signal of obliquity and/or precession.

Deep-time age models (e.g., Pre-Pleistocene) often rely on imprints of frequencies in sedimentary records that originate from the dynamics of the solar system orbits such as eccentricity and so-called *g*/*s*-modes (see below, e.g., 405, 173, and ~100 kyr; e.g., Berger et al., 1989; Cramer et al., 2003; Hilgen et al., 2010; Kocken et al., 2019; Lantink et al., 2019; Lauretano et al., 2018; Li et al., 2018; Lourens et al., 2005; Ma & Li, 2020; Vahlenkamp et al., 2020; Zeebe & Lourens, 2019; Zeeden et al., 2014). However, the use of obliquity and precession cycles (at present ~41 and ~20 kyr) remains challenging for these periods, primarily due to past changes in Earth's dynamical ellipticity and tidal dissipation, which affect the calculations (e.g., Laskar et al., 1993; Lourens et al., 1996, 2001; Quinn et al., 1991; Zeeden et al., 2013, 2014) but are difficult to reconstruct.

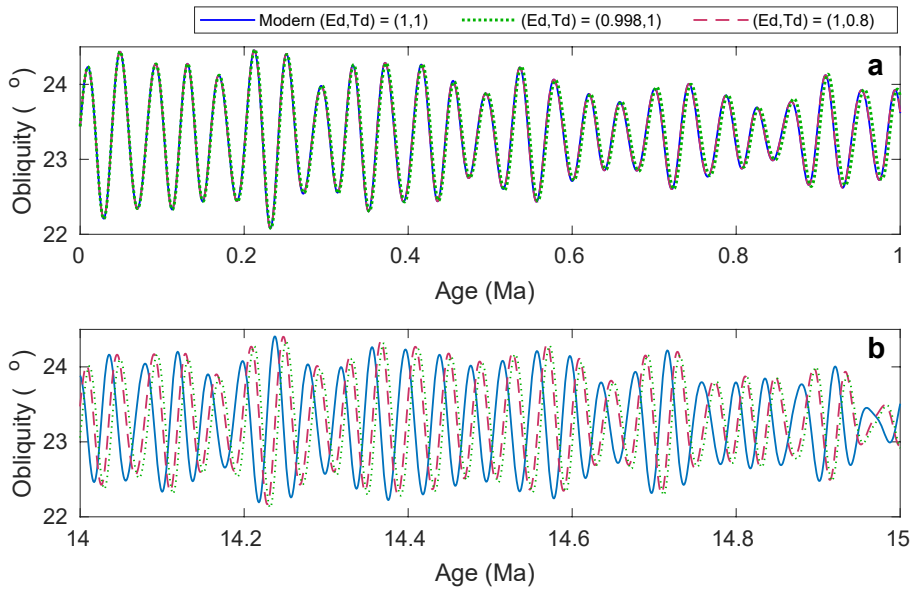

Figure 1. Illustration of changes in Earth's dynamical ellipticity (E_d) and tidal dissipation (T_d) affecting the numerical solution for Earth's obliquity (tilt axis) over 15 Myr. In runs labeled $E_d = 0.998$ and $T_d = 0.8$, the values of E_d and T_d were set to 80% and 99.8%, respectively, of their modern values ($E_d = T_d = 1.0$). For definitions of T_d and E_d as used here, see Section 2.4. (a) 0–1 Ma, the solutions are nearly identical. (b) 14–15 Ma, the solutions are out of phase, which would cause significant dating errors.

Early geological and geophysical analyses have focused mainly on tidal dissipation in the geologic past, including paleontological clocks from which changes in Earth's spin and the Moon's mean motion may be derived (for summary, see e.g., Deines & Williams, 2016; Lambeck, 1980; Montenari, 2018; Williams, 2000). Berger and Loutre (1994, BL94 hereafter) and Berger et al. (1989) estimated values for the precessional parameter (k, see Section 2.1) and obliquity and precession frequencies over the past 2.5 Gyr. BL94's calculations considered changes in the lunar orbit (Lambeck, 1980), length of day (LOD; Stoyko, 1970), and dynamical ellipticity values based on a geophysical model (Denis, 1986; past 440 Myr) or deduced from Walker and Zahnle (1986; past 2.5 Gyr). Note that Berger et al.'s calculations were based on quasi-periodic approximations of solar system solutions, not full numerical integrations as will be used in the present study (Zeebe, 2017; Zeebe & Lourens, 2019). BL94's results for, for example, the LOD (~22.7 hr at 250 Ma) are broadly compatible with observational evidence and cyclostratigraphy (Montenari, 2018; Williams, 2000) but differ from Laskar et al. (2004; LOD ~22.0 hr at 250 Ma), which assumes a stronger tidal dissipation rate that is closer to the modern value. For recent summaries on reconstructions of LOD, Earth-Moon distance, obliquity, and precession frequencies in the distant geologic past, see for example, Montenari (2018).

Focusing on the more recent past and using full numerical, astronomical solutions (as employed here), Quinn et al. (1991), for example, performed a numerical integration of the eight planets and Pluto and Earth's spin axis over the past ~3 Myr, including changes in tidal dissipation. Laskar et al. (1993) provided routines to calculate obliquity and precession from the output of their orbital solutions, including E_d and T_d parameters. For the same E_d and T_d values, the results of Laskar et al. (1993) and Quinn et al. (1991) were in very good agreement (cf. also, Touma & Wisdom, 1994). Notably, the precession-tilt (PT) solution is rather sensitive to changes in E_d. For instance, two obliquity solutions with $E_d = 1$ (present) vs. $E_d = 0.9977$ (which may occur during an ice age) show significantly different phases and amplitudes after 3 Myr of integration (Laskar et al., 1993; Lourens et al., 1996). Lourens et al. (2001) and Pälike and Shackleton (2000) fit E_d and T_d parameters to Ocean Drilling Program (ODP) Leg 154 data (past 25 Myr) and to a record from the Mediterranean Sea (past 3 Myr), respectively. These studies suggested that E_d and T_d varied by respectively +0.1/ −0.4‰ and +2.5/ −5.5% (past 25 Myr) and E_d by ±0.3‰ (past 3 Myr). However, note that it was later suggested that the ODP Leg 154 chronology requires revision and that the E_d bounds given by the two studies constitute a geophysical enigma (Morrow et al., 2012; Zeeden et al., 2013, 2014). Using the same approach but keeping $E_d = 1$ constant, ranges of T_d between 0.95 and 1.2 have been inferred over the past 12.5 Ma (Hüsing et al., 2007; Zeeden et al., 2014). Note that effects of

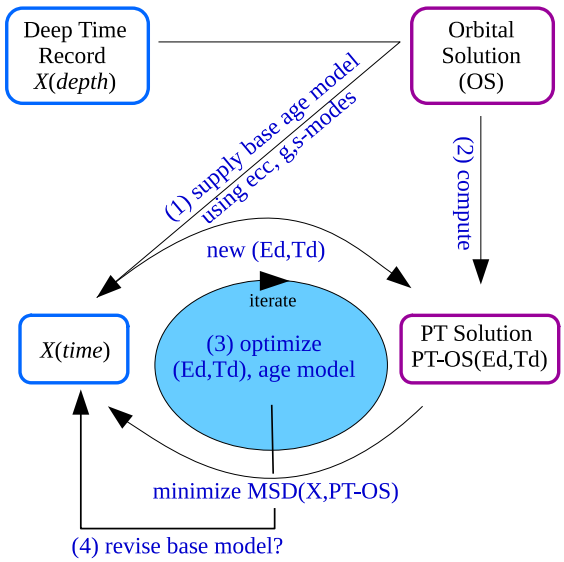

Figure 2. Schematic overview of our dating approach for sedimentary deep-time records. (1) For the data record in the depth domain $X(z)$, radiometric dates (if available) and the orbital solution (OS, e.g., ZB18a, Zeebe & Lourens, 2019) supplies a base age model using eccentricity and/or g, s-modes (see below), which provides the data record in the time domain, $X(t)$. (2) We compute the precession-tilt (PT) solution for a given OS and given initial values of dynamical ellipticity (E_d) and tidal dissipation (T_d), yielding a first guess for the combined precession-tilt-orbital solution, PT-OS(E_d, T_d). (3) We optimize the parameters E_d and T_d by minimizing the mean square deviation (MSD) between $X(t)$ and PT-OS(E_d, T_d) through iteration (note that multiple combinations for E_d and T_d may be possible, see text). The final PT-OS(E_d, T_d) supplies the optimized age model, E_d and T_d for a given base age model. (4) Depending on the results for E_d and T_d, the base model may require revision (see text).

so-called "climate friction" on obliquity were likely small over the past 50 Myr (see Levrard & Laskar, 2003 and references therein).

A value for the precessional parameter $k = 51.28 \pm 1.03$ arcsec yr^{-1} (2σ) has been estimated for the early Eocene (~55 Ma) using a cyclostratigraphic/statistical approach (Meyers & Malinverno, 2018). Setting $E_d = 1$, the result is consistent within 2σ with the present (50.38 arcsec yr^{-1}, Capitaine et al., 2003) and calculated value at 55 Ma (51.99 arcsec yr^{-1}) using modern T_d (Laskar et al., 2004). Geophysical modeling predicted up to −11‰ changes in dynamical ellipticity over the past 20 Myr (Forte & Mitrovica, 1997). However, using updated mantle viscosities (e.g., Lau et al., 2016; Mitrovica & Forte, 2004), the value was reduced to ca. ±1.5‰ over the past 25 Myr (Morrow et al., 2012). Explicit ocean tidal modeling suggests substantially lower T_d rates in the past, with an average $T_d \simeq 0.5$ over the past 50 Myr (see Green et al., 2017 and references therein). Note that the largest fraction of tidal energy is dissipated in the ocean, smaller fractions in the solid earth and atmosphere (e.g., Ray et al., 2001).

In summary, constraints on past E_d and T_d values are available, yet some with significant uncertainties. Below we will use some of the existing constraints and add new ones based on deep-time age model development (which is our primary goal here, not refining past E_d and T_d values). Our main motivation is the integration of E_d and T_d into astrochronology for the purpose of accurate deep-time dating and calibrating the ATS, which is hitherto missing.

2. Overview of Dating Approach

We illustrate our dating approach for sedimentary deep-time records by subdividing the task into several steps (Figure 2). Step 1: Given a data record in the depth domain, $X(z)$, radiometric dates (if available) and our astronomical solution (i.e., orbital solution, OS, such as ZB18a, see Zeebe & Lourens, 2019) supplies a base age model for the data record in the time domain, $X(t)$, using signals of eccentricity and/or other solar system frequencies in the record. Note that such signals may be detected directly or indirectly, for example, via amplitude modulation (AM). For example, the AM (or envelope) of precession is eccentricity (ultimately controlled by the solar system's fundamental g-modes, see below), while the AM of obliquity (axial tilt) is controlled by s-modes. Critically, however, the solution for the pure orbital motion of the solar system and hence eccentricity/g, s-modes (see below) are largely independent of Earth's obliquity and precession over the timescale considered here (see Zeebe, 2017). Conversely, the PT solution, however, does depend on the orbital solution. Thus, once the orbital solution has been obtained (computationally expensive), various PT solutions can be generated for this solution, for example, depending on parameters such as E_d and T_d (computationally inexpensive). See Section 2.4 for the definitions of E_d and T_d as used here.

In step 2, we compute the PT solution for a given OS and given initial values of E_d and T_d, yielding a first guess for the combined PT-orbital solution, dubbed PT-OS(E_d, T_d) (see Figure 2). In step 3, we optimize the parameters E_d and T_d by minimizing the mean square deviation (MSD, see Equation 1 below) between $X(t)$ and PT-OS(E_d, T_d). The final PT-OS(E_d, T_d) supplies the optimized age model and optimized values of E_d and T_d for a given base age model. Finally, if the optimized E_d and T_d values turn out to be beyond physically meaningful ranges, then the base age model may require revision in Step (4) (see, for example, Section 4.2). Also note that multiple combinations for E_d and T_d may be possible that minimize the MSD. In that case, our approach provides meaningful parameter bounds for both E_d and T_d. Importantly, our primary goal is age model development and (secondary) providing constraints (boundaries) for values of dynamical ellipticity and tidal dissipation for certain time intervals in the past and integrate those into our dating tool. Our approach is not designed to derive highly accurate time series for E_d and T_d in the past.

For this study's optimizations involving obliquity and precession cycles, we use the MSD:

$$\mathrm{MSD}(\tau) = \sum_{i=1}^{N_t} [X'(t_i - \tau) - s'(t_i)]^2 / N_t, \quad (1)$$

where X' and $s' = s'(t_i, E_d, T_d)$ are the values of the normalized data record and the astronomical PT-OS solution at time t_i, respectively, and τ is a time offset (when optimized, τ minimizes the MSD for a given combination of E_d and T_d values). The normalization includes demeaning, linearly detrending, and dividing by their respective standard deviation. For consistency with notations in previous studies (e.g., Zeebe & Lourens, 2019), we will also use the root MSD below (RMSD = $\sqrt{\mathrm{MSD}}$).

2.1. Solar System Frequencies

The g- and s-modes mentioned above are the fundamental frequencies of the orbital motion of the solar system bodies, obtained from solar system integrations and subsequent time-series analysis of the classic variables:

$$h = e \sin\varpi \quad ; \quad k = e \cos\varpi \quad (2)$$

$$p = \sin(I/2) \sin \Omega \quad ; \quad q = \sin(I/2) \cos \Omega, \quad (3)$$

where e, I, ϖ, and Ω are eccentricity, inclination, longitude of perihelion, and longitude of ascending node, respectively; for details, see for example Zeebe (2017); Zeebe and Lourens (2019). Combinations of individual g- or s-frequencies lead to AM of orbital parameters with characteristic periods, some of which can be identified in Earth's sedimentary records (AM is often called a "beat" in music). The precessional parameter k is related to the precession period of Earth's spin axis of ~25.7 kyr, or $k \simeq 50.38$ arcsec yr^{-1} at present (Capitaine et al., 2003), also called lunisolar precession. The combinations of k and g-frequencies result in the precession cycles observed in paleo-archives (~19–24 kyr).

2.2. Orbital Solutions

Orbital solutions were obtained from solar system integrations following our earlier work (Zeebe, 2015a; Zeebe, 2015b; Zeebe, 2017; Zeebe & Lourens, 2019) with the integrator package HNBody (Rauch & Hamilton, 2002) (v1.0.10) using the symplectic integrator and Jacobi coordinates (Wisdom & Holman, 1991; Zeebe, 2015a). All simulations include contributions from general relativity, available in HNBody as Post-Newtonian effects due to the dominant mass. The Earth-Moon system was modeled as a gravitational quadrupole (Quinn et al., 1991; lunar option), shown to be consistent with expensive Bulirsch-Stoer integrations up to 63 Ma (Zeebe, 2017). Initial conditions for the positions and velocities of the planets and Pluto were generated from the DE431 ephemeris (Folkner et al., 2014) using the SPICE toolkit for Matlab. The integrations for ZB18a included 10 asteroids, with initial conditions generated at ssd.jpl.nasa.gov/x/spk.html. The 10 asteroids were treated as heavyweight particles in HNBody, subject to the same full interactions as the planets. Coordinates were obtained at JD2451545.0 in the ECLIPJ2000 reference frame and subsequently rotated to account for the solar quadrupole moment (J_2) alignment with the solar rotation axis (Zeebe, 2017). Earth's orbital eccentricity and inclination from ZB18a is available at www2.hawaii.edu/~zeebe/Astro.html and www.ncdc.noaa.gov/paleo/study/26970. We provide results from 100 to 0 Ma but caution that the interval 100–58 Ma is unconstrained due to dynamical chaos in the solar system. Note that up-to-date orbital solutions disagree before ~50 Ma due to chaos (see, e.g., Zeebe, 2017), yet constraints on orbital solutions have recently been provided for the interval 58–50 Ma based on geologic data (Zeebe & Lourens, 2019).

2.3. PT Solutions

Our PT solutions are based by default on the orbital solution ZB18a (see above), which has been tested against, and shows exceptional agreement with, geologic data (Zeebe & Lourens, 2019). However, we have also computed PT solutions based on available orbital solutions from other authors such as La10x (Laskar, Fienga, Gastineau, & Manche, 2011; see Section 4.2). To compute the PT-solutions, we have implemented numerical routines in C that derive the obliquity and precession angle over time from the motion of the normal to Earth's equator (spin axis vector) around the instantaneous orbit normal vector (perpendicular to the instantaneous orbit plane; e.g., Bills, 1990; Goldreich, 1966; Quinn et al., 1991; Ward, 1974, 1979). Our code and pre-computed PT-solutions

are freely available at www2.hawaii.edu/~zeebe/Astro.html and www.ncdc.noaa.gov/paleo/study/35174. Our routines provide flexibility for numerical input (various orbital solutions), output, and ensemble integrations on computer clusters.

2.4. Dynamical Ellipticity and Tidal Dissipation

Dynamical ellipticity and tidal dissipation parameters as used in this study are defined as follows. Dynamical ellipticity refers to the gravitational shape of the Earth, largely controlled by the hydrostatic response to its rotation rate. Dynamical ellipticity is defined as $H = [C - (A + B)/2]/C = (C - A)/C$ (if $A = B$), where C is the polar moment of inertia and A and B are the equatorial moments of inertia. H is proportional to ω^2, where ω is Earth's spin (angular velocity). The present value of H is ~0.003 28; however, its precise, absolute value is usually adjusted to other parameters and hence may differ between models (e.g., Chen et al., 2015; Laskar et al., 1993; Quinn et al., 1991). As a result, a non-dimensional, effective parameter at time t, relative to the modern value (index "0") is often used—as is here, denoted as:

$$E_d = (H/\omega)_t/(H/\omega)_0, \tag{4}$$

with E_d values being close to 1.0. Note that the calculated changes in obliquity and precession in the past are sensitive to even small changes in E_d (see Sections 1, 4.1 and 5.2).

Tidal dissipation refers to the energy dissipation in the earth and ocean, which reduces Earth's rotation rate and increases the LOD and the Earth-Moon distance. Note though that the observed LOD change over, for example, the past 2,700 yr is less than expected from tidal friction, probably partly due to changes in E_d from post-glacial rebound (Stephenson et al., 2016). The parameter relevant here for the precession-obliquity solution is the change in lunar mean motion n (average angular frequency), which is presently decreasing at a rate:

$$Q_0 = (dn/dt)_0/n_0 = -4.6 \times 10^{-18} \ \ \mathrm{s}^{-1} \tag{5}$$

(Quinn et al., 1991). In this study, we use a non-dimensional, effective parameter at time t, also relative to the modern value, denoted as:

$$T_d = Q_t/Q_0. \tag{6}$$

For example, $T_d = 0.5$ means a tidal dissipation rate of half the modern value. The combined PT-orbital solution is denoted as PT-OS(E_d,T_d) (see Figure 2). For example, ZB18a(1, 1) refers to the orbital solution ZB18a with modern values $E_d = 1$ and $T_d = 1$. Note that by default, additional long-term effects of tidal dissipation on obliquity (secular trend) were not included here. However, the provided C code includes this option, following Quinn et al. (1991).

Theoretically feasible ranges of E_d and T_d may be estimated from the literature and first principles. For example, over the past 45 Myr recent studies that include glacial isostatic adjustment suggest maximum E_d changes (during the large Pleistocene ice age cycles) of about −1.5 to +0.5‰ and −2.0 to +0.5‰ from glacial surface loading (e.g., Farhat et al., 2021; Ghelichkhan et al., 2021; Morrow et al., 2012). This translates to E_d values ranging from ~0.9980 to ~1.0005. Recent geophysical models of the relative perturbation in E_d due to mantle convection based on different viscosity models suggest maximum changes of about ±2‰ over the past 50 Myr (E_d range ~0.9980 to ~1.0020; e.g., Ghelichkhan et al., 2021; Morrow et al., 2012). Based on first principles (e.g., Goldreich, 1966; Lambeck, 1980; Touma & Wisdom, 1994) and reconstructions of tides and the evolution of the Earth-Moon system, it is unlikely that long-term T_d values in the past were larger than the modern value (e.g., Berger et al., 1989; Green et al., 2017; Montenari, 2018; Walker & Zahnle, 1986; Williams, 2000). Thus, a possible range for T_d in the past is between zero and 1.0, although values close to zero appear unlikely.

3. Quickstart Guide: A Synthetic Record

To illustrate our method and provide a quickstart guide for users, we provide an easy-to-follow example using a synthetic record. Assume a simple orbital forcing, consisting only of long eccentricity (405 kyr) and tilt (~40 kyr) components, plus noise $\mathcal{N}$:

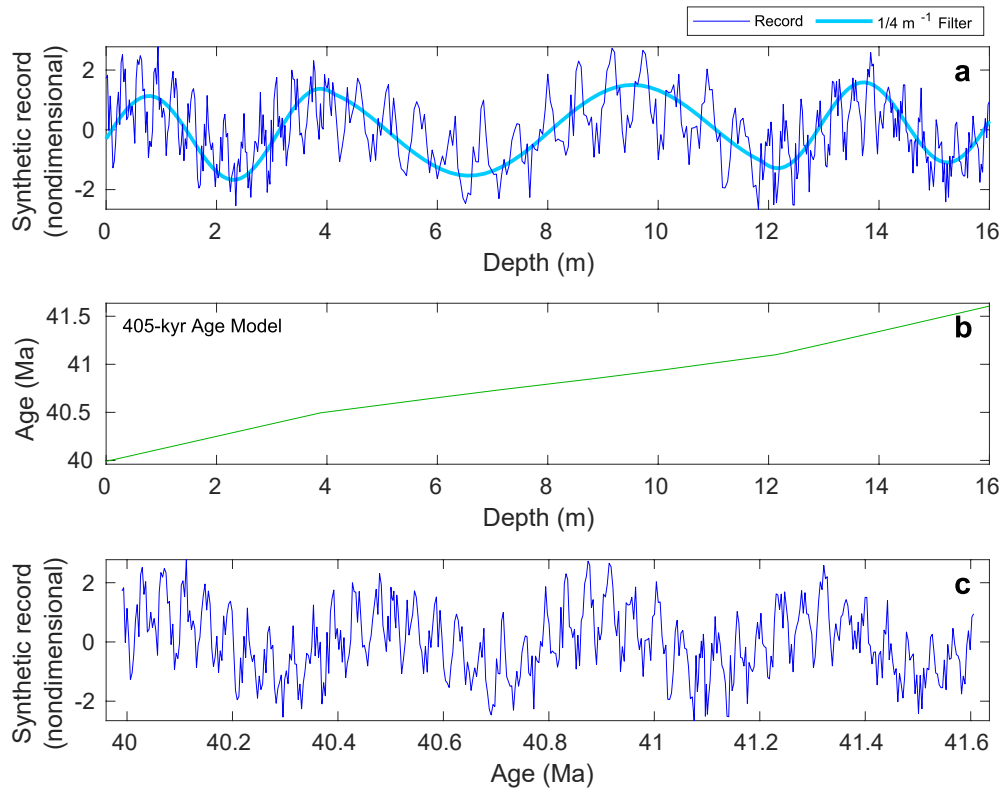

Figure 3. Illustrating the approach. (a) A synthetic record based on Equation 7, distorted in the depth domain. Light-blue line: 1/4 m^{-1} Gaussian filter (bandwidth ±50%), representing long eccentricity cycles. The filter bandwidth should be selected wide enough so that the filter properly fits the record, despite the distortion. (b) Age-depth relationship derived based on 405-kyr age model (see text). (c) Undistorted record in the time domain.

$$y(t) = A_1\cos(2\pi t/405) + A_2\cos(2\pi t/40) + \mathcal{N}, \quad (7)$$

where $A's$ are amplitudes and time t is in units of kyr (t may be offset by some t_0). The noise ($-1 < \mathcal{N} < 1$) was generated using random values drawn from the standard uniform distribution at each time interval with mean ≃0. Assume further that the recording of the forcing is somewhat distorted, say in a sediment archive, due to a non-constant sedimentation rate (Figure 3a). We start with this synthetic, nondimensional record to illustrate the steps of our approach, as outlined in Figure 2. The purpose of the steps described below is to first construct an initial base age model using the 405-kyr cycle, second to extract the obliquity component from the record, and third to build a refined age model by optimizing E_d and T_d. The parameters of the synthetic record such as temporal resolution, length, absolute time anchor (age), etc., were selected to be broadly similar to the parameters of the actual records discussed later.

3.1. Step 1: Base Age Model

If the approximate time interval and one absolute time anchor (e.g., from stratigraphy, radiometric dates, etc.) are available, we can use the long-eccentricity cycle to build a 405-kyr age model. The 405-kyr cycle may be provided by an orbital solution, or be assumed constant, which is a good approximation in many cases (age <50 Ma). Suppose the record is anchored at 40 Ma. Using a 1/4 m^{-1} filter (Gaussian, bandwidth ±50%), the long eccentricity cycle can be identified, suggesting a duration of ∼4 long cycles, or about 1.6 Myr (Figure 3a). (The filter bandwidth should be selected wide enough so that the filter properly fits the record, despite the distortion.) Using the maxima and minima of the filter as tie points, the base age model is readily constructed, providing an age-depth relationship and sedimentation rates (∼1 cm kyr^{-1}, Figure 3b). The undistorted record in the time domain (Figure 3c) is nearly identical to the original forcing function (Equation 7). As expected, the spectrum

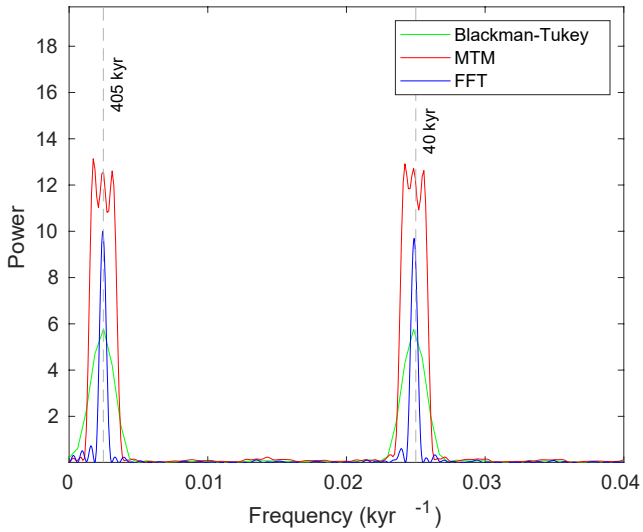

Figure 4. Spectral analysis of the undistorted record (Figure 3c). As expected, two lines dominate the spectrum at 405 and 40 kyr. The tiny offset of the 40-kyr line is due to the imperfect age model. Power spectra were computed using the Blackman-Tukey method, Fast Fourier Transform (FFT), and the multitaper method (MTM) with $K = 3$ tapers, where $K = 2p - 1$ and $p = 2$ is the time-bandwidth product.

of the undistorted record (Figure 3c) is dominated by two lines at 405 and 40 kyr (Figure 4), except for a tiny offset because of the imperfect age model.

Note that the temporal resolution of the synthetic record was set to $\Delta t = 3.2$ kyr ($N = 501$). For the resulting 1.6-Myr time series, the highest and lowest (Nyquist and Rayleigh) frequencies are hence $f_N = 1/(2\Delta t) = 0.156\ 25$ kyr^{-1} and $f_R = 1/(N\Delta t) = 0.625$ Myr^{-1}, corresponding to periods of 6.4 kyr and 1.6 Myr. Obliquity at ~40 kyr is hence well resolved. Also note that the synthetic age model construction was kept simple for illustration purposes. For actual records, the 405-kyr cycle should be provided by an astronomical solution (such as ZB18a), the time offset between floating chronology and solution be optimized, hiatuses, condensed sections, and dissolution intervals be considered carefully, etc. (see e.g., Zeebe & Lourens, 2019).

3.2. Step 2: PT Solution

Next, we focus on the obliquity component and its match with the PT solution. We extract the tilt component in the time domain using a 1/40 kyr^{-1} filter (Gaussian, bandwidth ±30%, Figure 5a). Note that in this case, the synthetic noise only has a small effect on the filter outcome, which may be different for actual records. At this stage, one can already guess some characteristics required of the PT solution to match the filtered record. Across the 1.6-Myr interval, the number of obliquity cycles in the filter is $N_T = 40$, that is, a period of ~40 kyr as expected (Figure 5a). For $N_T = 39$ and 41, the

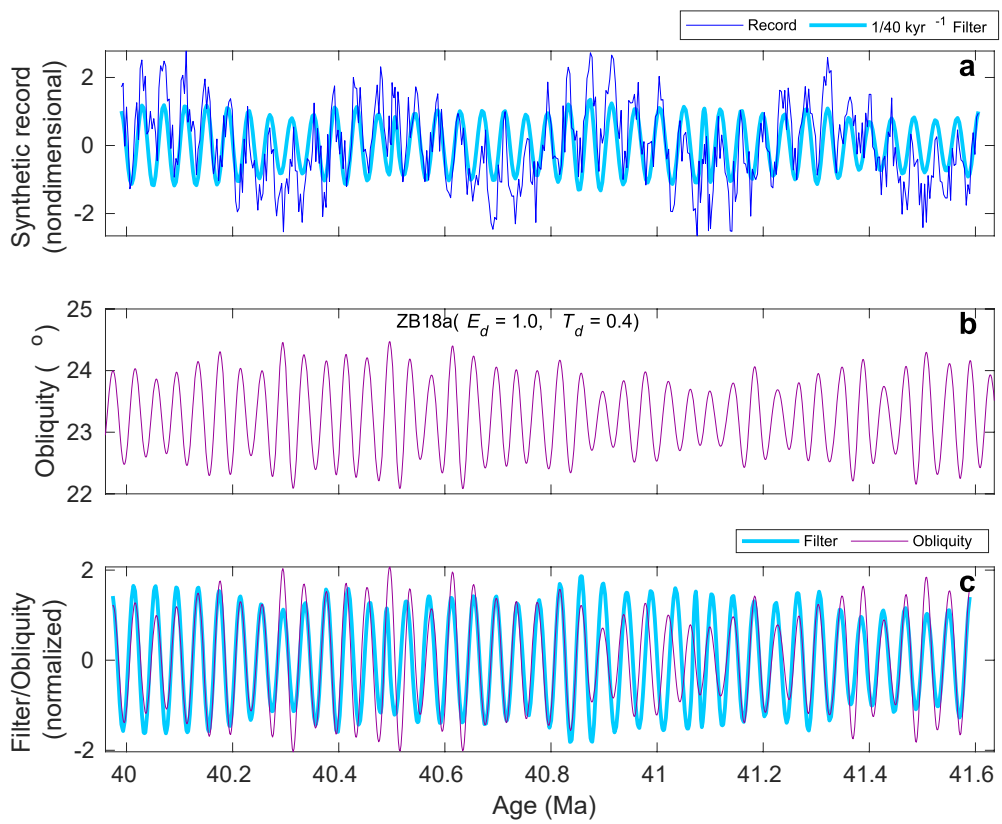

Figure 5. Matching the synthetic record with a precession-tilt solution. (a) Extraction of the tilt component in the time domain using a 1/40 kyr^{-1} Gaussian filter (bandwidth ±30%). (b) Precession-tilt orbital solution ZB18a ($E_d = 1.0$, $T_d = 0.4$). (c) Normalized filter (time offset τ optimized, see Equation 1) and normalized solution.

Table 1
MSD[a] for the Synthetic Record Based on ZB18a(E_d, T_d)

	T_d								
E_d	0.0	0.2	0.3	0.4	0.5	0.6	0.7	0.8	1.0
1.00	0.95	0.54	0.43	0.43	0.44	0.61	0.75	1.04	1.55

[a]Mean square deviation (Equation 1) between normalized, filtered record and normalized solution (see Figure 5c).

corresponding periods would be ~41 and ~39 kyr. The dominant obliquity period (P_T) over the past few million years is closer to $P_T \simeq 41$ kyr and hence it is already clear that, for instance, using values of $E_d = 1$ (modern) and $T_d = 0$ (no tidal dissipation) will not yield the desired match (41 kyr is too high, the frequency too low). Focusing only on T_d while keeping $E_d = 1$ constant, the solution ZB18a(1, 1) around 40 Ma yields $P_T = \sim 39.5$ kyr, which is too low (frequency is too high). Thus, the desired T_d target value must be between 0.0 and 1.0, perhaps somewhere around 2/3 (if the T_d-P_T relationship was linear, which it is not, then a change of 2/3 in T_d would correspond to the desired change of ~1 kyr in P_T, as $(41 - 39.5) \cdot 2/3 = 1$).

3.3. Step 3: Optimize E_d and T_d

In step 3, we compute the PT-solution ZB18a(E_d, T_d) for a variety of E_d and T_d values and evaluate the MSD between the normalized filtered record and the normalized solution (see Equation 1 and Table 1). For a systematic search for optimal E_d and T_d values to match actual records, our numerical routines and pre-computed PT solutions are freely available to users at www2.hawaii.edu/~zeebe/Astro.html and www.ncdc.noaa.gov/paleo/study/35174. It turns out that for the synthetic example, the solution ZB18a(1, 0.4) provides a good match with the filtered record (Figures 5b and 5c), with an MSD of 0.43 (Table 1). Focusing only on T_d while keeping $E_d = 1$ constant, the range $T_d \simeq 0.3$–0.5 appears feasible. While other combinations such as, for example (1.01, 0), also yield a small MSD, the key result is that all such solutions provide equally accurate age models as (1, 0.4) (Figure 5c), regardless of whether E_d and T_d are known individually. However, no conclusions can be drawn about the exact values of E_d and T_d, unless another independent constraint is provided for either one of them.

The good match between record and solution and the not too unrealistic range for T_d at $E_d = 1.0$ would suggests that the base age model in this case is robust (for contrasting results, see Section 4.2). Hence, step 4 of our approach (revision of the base age model, see Figure 2) appears unnecessary. Note that $E_d = 1.01$ was arbitrarily picked above for illustration purposes, which is likely too high (see Section 4.1). Yet, a lower E_d could be combined with a higher T_d to yield a very similar result, illustrating the indeterminacy of E_d and T_d as derived from astronomical solutions.

4. Case Studies

In the following, we demonstrate the practical utility of our approach by applying our dating tool to two case studies using deep-sea records from the early and middle Eocene.

4.1. Early Eocene, ODP Site 1262

We have recently computed a new astronomical solution (ZB18a), showing exceptional agreement with data records from ~58 to 53 Ma, which provides an absolute astrochronology up to 58 Ma and a new Paleocene-Eocene boundary age with a small margin of error (56.01 ± 0.05 Ma; Zeebe & Lourens, 2019). Our study used data from Walvis Ridge ODP Site 1262 in the South Atlantic and generated a new age model for Site 1262 based on the remarkable expression of 405- and ~100-kyr eccentricity cycles in color reflectance (a*-1262). Note that while the long 405-kyr eccentricity cycle is nearly stable over the considered time interval, the short 100-kyr eccentricity cycle is not (e.g., Laskar, Fienga, et al., 2011; Zeebe, 2017). Expression of the short eccentricity cycle in the geologic record allows selecting appropriate orbital solutions (Zeebe & Lourens, 2019). In the early Eocene (~55.6 to ~54.1 Ma), color reflectance at Site 1262 also shows a striking expression of climatic precession (~20 kyr cycles), which we use here as the first case study to demonstrate our dating approach (see Figure 6).

We compare the observed and calculated precession cycles from Site 1262 and our PT solution based on ZB18a (Zeebe & Lourens, 2019). The relative chronology of the a*-1262 record (Figure 6a) is based on our original age model using only eccentricity cycles. For quantitative comparison with astronomical precession cycles, we applied a 20-kyr Gaussian filter (frequency bandwidth ±30%) to the a*-1262 record. Furthermore, we calculated the climatic precession for our astronomical solution ZB18a, starting with modern parameter values $E_d = 1$ and $T_d = 1$ (Figure 6b). The climatic precession is $e \sin \varpi$, where e is the eccentricity and ϖ is the longitude of

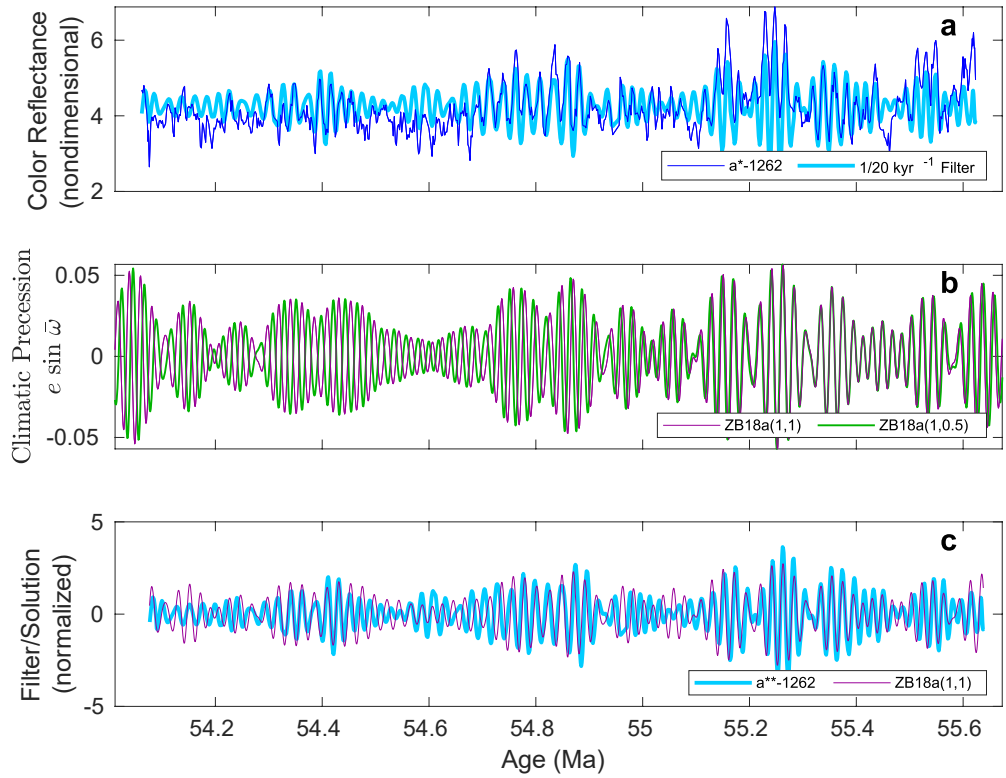

Figure 6. Data analysis and application of our dating approach to deep-time records (case study 1): Color reflectance a^* at ODP Site 1262 (indicating lithology changes). (a) a^*-record and 20-kyr filter. (b) Climatic precession ($e \sin \varpi$) for our astronomical solution ZB18a (Zeebe & Lourens, 2019), where e is eccentricity and ϖ is the longitude of perihelion from the vernal equinox (see e.g., Berger & Loutre, 1994). ZB18a(1, 1) indicates $E_d = 1$, $T_d = 1$. (c) Normalized filter a^{**}-1262 and normalized solution (see text).

perihelion from the vernal equinox, see for example, Berger and Loutre (1994). Next, both filter and solution were normalized, that is, demeaned, linearly detrended, and normalized to their respective standard deviation. Finally, we optimized the offset between filter and solution by shifting the filtered a^*-1262 record along the time axis (offset τ) over a time interval of ±60 kyr (approximately ±3 precession cycles) to find the minimum MSD (see Equation 1) between the filtered, normalized record (a^{**}-1262) and the normalized astronomical solution. In other words, we allow for potential offsets between data and astronomical solutions with different E_d and T_d values, as E_d and T_d shift both phase and period of the precession cycles. For small MSDs, the optimum offset for Site 1262 turned out to be only 10–15 kyr.

Table 2
MSD[a] for the a-1262 Record Based on ZB18a(E_d, T_d)*

	T_d							
E_d	0.0	0.5	0.7	0.8	0.9	1.0	1.1[b]	1.2[b]
1.000	1.47	1.29	1.03	0.94	0.89	0.95	0.96	1.12
0.998	1.45	1.39	1.11	1.04	0.92	0.89		
1.005	1.52	1.05	0.92	0.89	0.95	1.08		
1.012[b]		0.89						

[a]Mean square deviation between normalized filtered record and normalized solution ZB18a(E_d, T_d) (Figure 6c). [b]Values are physically unrealistic or unlikely (included for illustration only).

4.1.1. Varying E_d and T_d

The agreement between a^{**}-1262 and normalized ZB18a(1,1) both in terms of frequency and AM appears excellent considering that we compare a ∼55 Myr old sedimentary record and a solution with modern parameter values $E_d = 1$ and $T_d = 1$ (Figure 6b), which yields a small MSD (see Table 2). The agreement is particularly remarkable because orbital solutions disagree before ∼50 Ma due to dynamical chaos in the solar system (see, e.g., Zeebe, 2017). Our analysis here is based on the solution ZB18a, which represents a single realization of the solar system's evolution and shows exceptional agreement with geologic data up to ∼58 Ma, for example, with the 1262-eccentricity record (Zeebe & Lourens, 2019). For the same E_d and T_d parameter values, other solutions yield MSDs that are larger than those for ZB18a (see Section 5.2.1). An even (slightly) smaller MSD can be obtained for ZB18a(1, 0.9). For comparison, MSD ≃ 1.47 for ZB18a(1, 0). The latter result illustrates one significant advantage of using deep-time records over

younger records. For instance, the effect of changes in T_d on the PT solution become so large over 55 Myr that solutions with $T_d = 1$ vs. $T_d = 0$ are clearly distinguishable (~60% difference in MSD). In contrast, the two solutions are virtually indistinguishable over 3 Myr (cf. also, Lourens et al., 2001).

Fixing the tidal dissipation at $T_d = 1$ and varying E_d, a slightly better fit to the filtered a*-1262 record can be obtained for $E_d = 0.998$ (Table 2). However, even for ZB18a(1, 1) the match in AM (due to eccentricity), as well as total number of precession cycles (N_P) between the filtered record and the solution appears remarkable, given modern E_d and T_d parameter values (see Section 4.2 for contrasting results). For example, across the interval, $N_P = 75$ or 76 for a*-1262 (slightly depending on filter width) and $N_P = 74$ for the astronomical solution, that is, a difference of only 1–2 precession cycles over 1.56 Myr (although see Section 4.1.3 for important notes on N_P). At a precession period of approximately 20 kyr, this indicates a dating error of only 20–40 kyr (1.3%–2.6% of the interval duration). The error could be slightly larger due to uncertainties in the phasing between precession forcing and a* and/or uncertainties in the base age model (see Section 5.3). Nevertheless, the error is much smaller than preliminary results for a middle Eocene record from the North Atlantic suggest (see Section 4.2).

From our optimized solution ZB18a(1, 0.9) for the a*-1262 record, we can also calculate the precessional parameter k around 55 Ma. We calculated k in two different ways. First, directly from the lunisolar precession (see Quinn et al., 1991) averaged across the interval. Second, from a spectral analysis (Fast Fourier Transform, FFT) of the precession solution across the interval. For the latter approach, we used the precession frequency $p_1 = k + g_5$, where p_1 was obtained by FFT and g_5 is a solar system frequency mostly related to Jupiter's orbit (essentially stable, see Section 5.2.1). The two approaches yielded consistent results, that is, 51.63 and 51.60 arcsec yr^{-1}, respectively (periods of 25.10 kyr and 25.11 kyr). While the inferred frequency for k at ~55 Ma is significantly higher than the modern value, no firm conclusion can be drawn from this about the individual evolution of E_d and T_d (see Section 5.2).

4.1.2. Combining Precession and Eccentricity

Importantly, we can now combine the precession-based age model with an eccentricity-based 405- and 100-kyr age model using our astronomical solution (Zeebe & Lourens, 2019). The integration of precession and eccentricity also provides a check on whether or not any precession cycles are missing in the data record and provides an absolute dating accuracy which is likely as good or better than recent radiometric dating. For example, the absolute age uncertainty for the 1262 record at, say 55.00 Ma, then is 55.00 ± 0.02/0.04 Ma, given a robust base age model (for discussion, see Section 5.3). For comparison, reported systematic uncertainties for recent radiometric K/T boundary ages based on ^{40}Ar/^{39}Ar dating are about ±0.04 Ma to ±0.06 Ma but may be much larger when different calibrations are used (Kuiper et al., 2008; Renne et al., 2013; Sprain et al., 2018).

We have also calculated the MSD for ZB18a(1, 0.5) (see Table 2) as it has been suggested that $T_d \simeq 0.5$ over much of the past 50 Myr (Green et al., 2017). However, (E_d, T_d) = (1, 0.5) does not result in a good match with a**-1262, which would require $E_d = 1.012$, when assuming $T_d = 0.5$. A value of $E_d = 1.012$ (+12‰ relative to modern) appears significantly larger than changes suggested by geophysical models over the past 50 Myr. For example, numerical studies of the relative perturbation in E_d due to mantle convection based on different viscosity models suggest maximum changes of about ±2‰ over the past 50 Myr (e.g., Ghelichkhan et al., 2021; Morrow et al., 2012). Allowing $E_d = 1.005$ (+5‰ change) still does not result in a good match for $T_d = 0.5$, but would require $T_d \simeq 0.8$ (Table 2). In summary, based on our analysis of the a*-1262 record, estimated ranges for E_d and T_d are ~0.998 to ~1.005 and ~0.8 to ~1.0, respectively (although see Section 5.3). Critically, however, neither parameter can be determined more accurately, unless another independent constraint is provided for either one of them.

4.1.3. Note on Frequency and Total Cycles

The relationship between T_d (for E_d = const.) and an average precession frequency (f_P) for an astronomical solution across a given interval is rather straightforward. However, in our analysis, the relationship between T_d and the total number of precession cycles (N_P) for the normalized and cropped solution is not. For example, say f_P is determined by spectral analysis of ZB18a(1, T_d) across a given interval (Figure 6b). Then f_P increases monotonically with T_d, because a stronger tidal dissipation results in a higher average precession frequency in the past. However, the relationship between T_d and N_P for the normalized and cropped solution (Figure 6c) is more complex. First, the exact shape of the solution at the eccentricity nodes (maximum, minimum, shoulder, inflection point, etc.; see, for example, Figure 6c around 55.1 Ma) is sensitive to changes in T_d and hence so is the number of maxima or

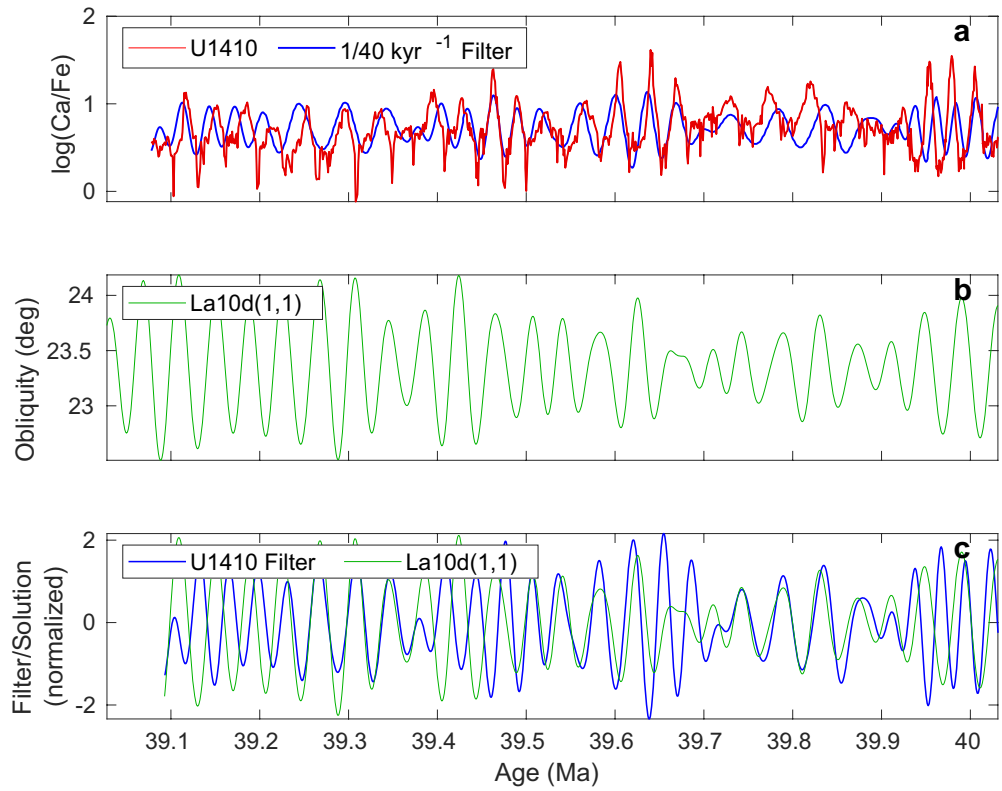

Figure 7. Data analysis and application of our dating approach to deep-time records (case study 2): Ca/Fe ratios at IODP Site U1410 (indicating lithology changes, Boulila et al., 2018). (a) Ca/Fe record (log) and 40-kyr filter. (b) Obliquity (in degrees) for the astronomical solution La10d (Laskar, Fienga, et al., 2011). La10d(1, 1) indicates $E_d = 1$, $T_d = 1$. (c) Normalized filter and solution (see text).

minima identified around the nodes. Second, because we also optimize the time offset τ between filter and solution (see Equation 1), small changes in T_d can shift the final interval (cropped at the edges) such that maxima or minima appear or disappear at the interval edges. As a result, there is no simple, monotonic relationship between T_d (E_d = const.) and N_P as determined by cycle counting using maxima or minima.

4.2. Middle Eocene, IODP Site U1410

A middle Eocene record from the North Atlantic (Site U1410) was recently recovered during IODP (Integrated ODP) Exp. 342 (Boulila et al., 2018, B18 hereafter; Cappelli et al., 2019; Norris et al., 2014). The basic lithological changes as recorded in Ca/Fe ratios were suggested to be driven by Earth's obliquity, with an AM of ~173 kyr (see Figure 7). The 173-kyr cycle originates from the solar system's fundamental frequencies s_3 and s_6 (loosely related to the ascending nodes of Earth's and Saturn's orbits). As a second illustration of our dating tool, we selected the interval from ~40 to ~39.1 Ma, which was highlighted in Figure 5 of B18 (see Figure 7a). We focus here on Site U1410, but note that our analysis gives very similar results for nearby Site U1408 (which appears to have a hiatus in an older part of the record at ~42 Ma).

For the base chronology of the Ca/Fe-U1410 record (Figure 7a), we use the original, published age model of B18. For quantitative comparison with astronomical obliquity cycles, we applied a 40-kyr Gaussian filter (bandwidth ±70%) to the Ca/Fe-U1410 record. This results in the same number of obliquity cycles ($N_T = 28$) across the interval as originally published in B18. Furthermore, we calculated Earth's obliquity for the astronomical solution La10d (Laskar, Fienga, et al., 2011), starting with modern parameter values $E_d = 1$ and $T_d = 1$ (Figure 7b). Note that B18's age model is based on $s3 - s6$ of the solution La11 (Laskar, Gastineau, Delisle, Farrés, & Fienga, 2011). To our knowledge, output to calculate the PT-solution for La11 is not available, which is of minor importance, however, as $s3 - s6$ seems identical for La11 and La10d across the interval (see Figure 2d in

B18). The match between the normalized filter and solution is poor for La10d(1, 1), that is, $E_d = 1$ and $T_d = 1$ (Figure 7c). Over the same interval (~900 kyr), the solution shows $N_T = 24$ obliquity cycles, whereas the filtered record suggests $N_T = 28$. At an obliquity period of approximately 40 kyr, this indicates a dating error of ~160 kyr (18% of the interval duration). Note that the error could be slightly larger due to uncertainties in the phasing between obliquity forcing and Ca/Fe ratios. In order to improve the match (both in terms of N_T and MSD), one would have to increase T_d to 6 ($E_d = 1$) or E_d to 1.1 ($T_d = 1$). A six-fold change in tidal dissipation or a 10% change in dynamical ellipticity relative to the modern appears very unlikely. This suggests that the original base age model for U1410 requires revision (cf. also, Cappelli et al., 2019; Vahlenkamp et al., 2020; Westerhold et al., 2019). Potential future work tackling this task could be aided by the dating tool introduced here.

5. Discussion

The primary motivation for the present study is the integration of dynamical ellipticity and tidal dissipation into astrochronology. Specifically, our approach aims at accurate deep-time age model development and calibration of the ATS utilizing dynamical ellipticity and tidal dissipation, which is hitherto missing.

5.1. Significance

Regarding the significance of accurate dating methods such as ours, we point out that the ability to provide absolute geologic ages and high-fidelity chronologies reaches far beyond mere archiving and cataloging of Earth's history. For example, accurate absolute ages of past climate-carbon cycle events relative to ages of forcings such as volcanism, impacts, orbital forcing, etc., are critical to understand drivers and triggers of climatic and environmental changes, catastrophes, etc. (e.g., Cramwinckel et al., 2018; Kump et al., 2009; Zachos et al., 2001). Moreover, the relative timing of events (detailed chronology) is essential to understanding both past changes in long-term climate and rapid climate events. The chronology of the early Eocene hyperthermals in relation to climate change, the evolution and dispersal of mammals (e.g., Bowen et al., 2002, 2001; Koch et al., 1992), and orbital forcing represents just one example (e.g, Lauretano et al., 2015; Lourens et al., 2005; Zeebe & Lourens, 2019; Zeebe et al., 2017). Hyperthermals, for instance, are considered the best paleo-analogs for massive carbon release and the climate response to anthropogenic carbon release (e.g., Bowen et al., 2006; IPCC, 2013; Kump et al., 2009; Zachos et al., 2005; Zeebe et al., 2016, 2009). However, understanding and projecting future climatic and environmental change informed by paleoclimate studies requires rigorous separation of past forcings—and hence accurate dating—to identify similarities and differences to present and future forcings.

5.2. Indeterminacy of E_d and T_d

Our analysis of the synthetic record and the a*-1262 record illustrates the indeterminacy of E_d and T_d as derived from astronomical solutions. While an accurate age model, the precessional parameter k (see Section 4.1.1), and ranges for E_d and T_d may be derived based on our approach, it does not yield precise, individual values for E_d and T_d in the past, unless another independent constraint is provided for either one of them. Unfortunately, we are therefore unable to draw any firm conclusions on, for instance, the evolution of tidal dissipation over the past ~55 Myr. With that caveat in mind, we note that our analysis of the a*-1262 record yields estimated ranges for E_d and T_d of ~0.998 to ~1.005 and ~0.8 to ~1.0, respectively (although see Section 5.3).

5.2.1. Effects of E_d, T_d, Orbital Solution, and Chaos on Obliquity and Precession

To evaluate the results for obliquity and precession presented here, it is important to understand their dependency on E_d, T_d, and the orbital solution. The latter is particularly relevant before ~50 Ma, where orbital solutions disagree due to solar system chaos. Fundamentally, obliquity and climatic precession are controlled by the precessional parameter k and the solar system frequencies (g's and s's, see Section 2.1). In turn, k is affected, for instance, by changes in E_d and T_d, while the g's and s's depend on the orbital solution. The dominant obliquity and precession frequencies are combinations of $k + s_i$ and $k + g_i$, respectively. Furthermore, the amplitudes of obliquity and climatic precession are modulated by the g's and s's (e.g., eccentricity is the envelope of climatic precession). Hence it is clear that differences in orbital solutions (say before ~50 Ma) influence both the dominant frequencies and the AM of obliquity and climatic precession via the g's and s's. To what extent, however, depends on whether the relevant g's and s's are stable, or are changing over time due to chaos.

Table 3
MSD and Selected Frequencies[a] for Different Precession-Tilt-Orbital Solutions, PT-OS(E_d, T_d)

	MSD[b]	$k + g_5$ (P)[c]	$k + s_3$ (T)[d]
		Period (kyr)	Period (kyr)
ZB18a(1, 1.0)	0.95	23.12	41.46
ZB18a(1, 0.1)	1.51	23.62	41.62
La10d(1, 1.0)	0.99	23.16	41.07
La10d(1, 0.1)	1.61	23.65	41.15

[a]There are several dominant precession/tilt frequencies; we only select two here for illustration. [b]Mean square deviation (Equation 1) between normalized, filtered 1262 precession record and normalized PT-OS (cf. Table. 2). [c]Precession (P) frequency $k + g_5$ (from Fast Fourier Transform) of PT-OS, interval 58–53 Ma. [d]Obliquity (tilt, T) frequency $k + s_3$ (from Fast Fourier Transform) of PT-OS, interval 58–53 Ma.

In the following, we exemplify the above effects focusing on ODP Site 1262 and the time interval 58–53 Ma (see Zeebe & Lourens, 2019). Also, we will only examine changes in T_d, which have a similar effect as changes in E_d. The MSD between the normalized, filtered 1262-precession record and the normalized PT-OS solution (cf. Table 2) shows a better fit for our solution ZB18a than for, for example, La10d (Laskar, Fienga, et al., 2011), regardless of E_d and T_d (Table 3). The better fit is primarily due to the overall AM of precession, that is, the more suitable eccentricity pattern of the orbital solution ZB18a (Zeebe & Lourens, 2019). In contrast, the values for one of the dominant precession frequencies ($k + g_5$) are similar for ZB18a and La10d across the interval 58–53 Ma at the same E_d and T_d (Table 3). The reason is that T_d has the same effect on k for both orbital solutions and that g_5 (mostly related to Jupiter's orbit) is essentially stable in both solutions. For the dominant obliquity frequency $k + s_3$, the orbital solution is more important, as g_3 (mostly related to Earth's orbit) is susceptible to chaotic dynamics and evolves differently in the two orbital solutions across the interval. In summary, E_d and T_d affect k in a straightforward manner. However, the orbital solution affects AM and dominant frequencies of obliquity and precession to varying extents, depending on whether or not the relevant g's and s's are impacted by chaos, that is, are stable or not.

5.3. Age Model Uncertainties, ODP Site 1262

The accuracy of the age model for Site 1262 using precession cycles (see Section 4.1) depends on the accuracy of the base age model using eccentricity cycles developed in Zeebe and Lourens (2019). For example, variations in the total interval duration of the base model could allow for a different number of total precession cycles, affecting the uncertainty of the precession-based age model. To test the dependency of the precession-based age model on the base age model, we have artificially distorted the depth coordinate of the base age model, which resulted in a degrading fit (increasing root MSD, RMSD) between the filtered a*-1262 eccentricity record and our astronomical solution ZB18a (see Figure 8). The distorted depth coordinate (z') was obtained by linearly stretching/contracting the original depth coordinate z using $z' = z + \delta \times (z - z_0)$, where δ is a small parameter (independent of depth, varied to obtain different RMSD) and z_0 is the top of the section in the depth domain (selecting the top of the section avoids filter distortion across the ETM-2, see Zeebe & Lourens, 2019). The base model tie points, however, were held at their original positions ($z'_{tp} = z_{tp}$), which hence resulted in small relative offsets between the tie point positions of the distorted record and the astronomical solution, compared to the original tie point positions and the astronomical solution (depending on the parameter δ). Note that the RMSDs calculated here are different from those in Zeebe and Lourens (2019) due to different interval lengths. For each base model with a given RMSD we have then calculated the fit (MSD) between the filtered precession record and the PT-solution ZB18a(1, 1).

First, the smallest RMSD also corresponds to the smallest MSD (see Figure 8), likely due to the fact (at least partly) that eccentricity is the envelope of precession, that is, eccentricity and precession are correlated for a given astronomical solution. Second, the calculated MSD increases only slightly up to a certain threshold RMSD but rapidly beyond that threshold. The filtered base records for RMSDs above the threshold provide visibly poor fits and are inferior compared to better fits with smaller RMSD. However, fits with RMSDs close to the minimum value could potentially be considered viable and would thus somewhat increase the uncertainty of the final precession-based age model at Site 1262 (compare Table 2).

5.3.1. Record Length

Another parameter that may affect the results of the precession-based age model is the record length. Regarding age model development, shorter records commonly yield less accurate results, as higher frequency fluctuations (which average out over long records) are more significant. We have tested the effect of the record length on the precession-based age model (and optimal E_d and T_d) at Site 1262 (see Section 4.1) by breaking the a*-1262 record down into various sub-sections (total length ~1.56 Myr), with at least half the interval length. Keeping $E_d = 1$ constant, it turned out that for intervals of $L_T \simeq 1$, ~1.2, and ~1.4 Myr (youngest age ~54 Ma for all), the optimal

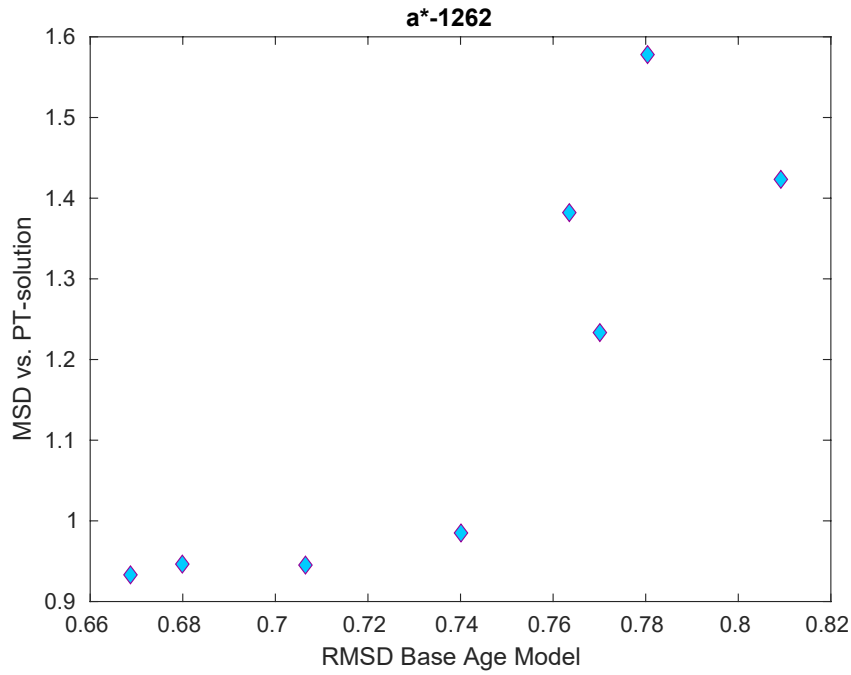

Figure 8. Evaluating age model uncertainties. Mean square deviation (MSD) between the filtered a*-1262 precession record and PT-solution ZB18a(1, 1) (see Figure 6c) plotted against the root mean square deviation (RMSD) between the filtered a*-1262 eccentricity record and ZB18a (base age model, see Zeebe & Lourens, 2019). Different RMSD for the base age model were obtained by artificially distorting the depth coordinate of the a*-1262-record (see text).

T_d is 0.9, the same as for the full record (cf. Table 2). For $L_T \simeq 790$ kyr, the optimal $T_d = 1.1$. Furthermore, at shorter L_T, the optimal T_d was found to be sensitive to small variations in L_T. This result emphasizes the advantage of using longer over shorter records (if available), which are usually also less sensitive to effects such as filter distortion at the interval boundaries.

6. Summary

In this study, we have presented an accurate dating method for deep-time records by integrating dynamical ellipticity and tidal dissipation into astrochronology. Our approach is based on the combination of constraints on T_d (and thus indirectly on E_d) with age model optimization based on solar system frequencies, including tuning to obliquity/precession frequencies, while varying T_d and E_d. We have targeted deep-time intervals where T_d shows significant effects but high-quality sedimentary records are available (early Cenozoic). We have applied our dating tool to two case studies using deep-sea records from the early and middle Eocene to demonstrate the practical utility of our approach. Our results confirm very accurate chronologies of sedimentary records from the early Eocene but suggest a significant improvement for the middle Eocene. We propose that potential future work tackling the middle Eocene ATS may use the dating tool introduced here. For the early Eocene, our method provides absolute geologic ages with an estimated uncertainty of ±20–40 kyr, which is smaller than or equal to typical uncertainties from recent radiometric ^{40}Ar/^{39}Ar dating.

Data Availability Statement

Our numerical routines in C and pre-computed PT solutions are freely available at www2.hawaii.edu/~zeebe/Astro.html and www.ncdc.noaa.gov/paleo/study/35174.

Acknowledgments
The authors thank Chao Ma, David Minton, and one anonymous reviewer for reviews, which improved the manuscript. We also thank Linda Hinnov for spotting an incorrect plot in one of the figures. This research was supported by U.S. NSF grants OCE20-01022, OCE20-34660, and Heising-Simons Foundation Grant #2021-2800 to R.E.Z. and grants from the Netherlands Organisation for Scientific Research (NWO-ALW 865.10.001) and the Netherlands Earth System Science Centre (NESSC 024.002.001) to L.J.L.

References

Berger, A., & Loutre, M. F. (1994). Precession, eccentricity, obliquity, insolation, and paleoclimates. In J.-C. Duplessy, & M.-T. Spyridakis (Eds.), *Long-term climatic variations* (pp. 107–151). Springer Berlin Heidelberg. https://doi.org/10.1007/978-3-642-79066-9_5

Berger, A., Loutre, M. F., & Dehant, V. (1989). Influence of the changing lunar orbit on the astronomical frequencies of pre-Quaternary insolation patterns. *Paleoceanography*, *4*(5), 555–564. https://doi.org/10.1029/PA004i005p00555

Bills, B. G. (1990). The rigid body obliquity history of Mars. *Journal of Geophysical Research*, *95*, 14137–14153. https://doi.org/10.1029/JB095iB09p14137

Boulila, S., Vahlenkamp, M., De Vleeschouwer, D., Laskar, J., Yamamoto, Y., Pälike, H., et al. (2018). Towards a robust and consistent middle Eocene astronomical timescale. *Earth and Planetary Science Letters*, *486*, 94–107. https://doi.org/10.1016/j.epsl.2018.01.003

Bowen, G. J., Bralower, T. J., Delaney, M. L., Dickens, G. R., Kelly, D. C., Koch, P. L., et al. (2006). The Paleocene-Eocene thermal maximum gives insight into greenhouse gas-induced environmental and biotic change. *Eos, Transactions American Geophysical Union*, *87*, 165–169. https://doi.org/10.1029/2006eo170002

Bowen, G. J., Clyde, W. C., Koch, P. L., Ting, S., Alroy, J., Tsubamoto, T., et al. (2002). Mammalian dispersal at the Paleocene/Eocene boundary. *Science*, *295*, 2062–2065. https://doi.org/10.1126/science.1068700

Bowen, G. J., Koch, P. L., Gingerich, P. D., Norris, R. D., Bains, S., & Corfield, R. M. (2001). Refined isotope stratigraphy across the continental Paleocene-Eocene boundary on Polecat Bench in the Northern Bighorn Basin. In P. D. Gingerich (Ed.), *Paleocene-Eocene stratigraphy and biotic change in the Bighorn and Clarks Fork Basins* (Vol. 33, pp. 73–88). University of Michigan Papers on Paleontology.

Capitaine, N., Wallace, P. T., & Chapront, J. (2003). Expressions for IAU 2000 precession quantities. *Astronomy & Astrophysics*, *412*, 567–586. https://doi.org/10.1051/0004-6361:20031539

Cappelli, C., Bown, P., Westerhold, T., Bohaty, S. M., de Riu, M., Lobba, V., et al. (2019). The early to middle Eocene transition: An integrated calcareous nannofossil and stable isotope record from the Northwest Atlantic Ocean (Integrated Ocean Drilling Program Site U1410). *Paleoceanography and Paleoclimatology*, *34*(12), 1913–1930. https://doi.org/10.1029/2019pa003686

Chen, W., Li, J. C., Ray, J., Shen, W. B., & Huang, C. L. (2015). Consistent estimates of the dynamic figure parameters of the Earth. *Journal of Geodesy*, *89*(2), 179–188. https://doi.org/10.1007/s00190-014-0768-y

Cramer, B. S., Wright, J. D., Kent, D. V., & Aubry, M.-P. (2003). Orbital climate forcing of δ^{13}C excursions in the late Paleocene-early Eocene (chrons C24n-C25n). *Paleoceanography*, *18*, 1097. https://doi.org/10.1029/2003PA000909

Cramwinckel, M. J., Huber, M., Kocken, I. J., Agnini, C., Bijl, P. K., Bohaty, S. M., et al. (2018). Synchronous tropical and polar temperature evolution in the Eocene. *Nature*, *559*(7714), 382–386. https://doi.org/10.1038/s41586-018-0272-2

Deines, S. D., & Williams, C. A. (2016). Earth's rotational deceleration: Determination of tidal friction independent of timescales. *The Astronomical Journal*, *151*(4), 103. https://doi.org/10.3847/0004-6256/151/4/103

Denis, C. (1986). On the change of kinetical parameters of the Earth during geological times. *Geophysical Journal*, *87*(2), 559–568. https://doi.org/10.1111/j.1365-246X.1986.tb06637.x

Farhat, M., Laskar, J., & Boué, G. (2021). *Constraining the earth's dynamical ellipticity from ice age dynamics*. arXiv:2103.14682.

Folkner, W. M., Williams, J. G., Boggs, D. H., Park, R. S., & Kuchynka, P. (2014). The planetary and lunar ephemerides DE430 and DE431. *Interplanetary Network Progress Report*, *196*, 1–81.

Forte, A. M., & Mitrovica, J. X. (1997). A resonance in the Earth's obliquity and precession over the past 20 Myr driven by mantle convection. *Nature*, *390*(6661), 676–680. https://doi.org/10.1038/37769

Ghelichkhan, S., Fuentes, J. J., Hoggard, M. J., Richards, F. D., & Mitrovica, J. X. (2021). The precession constant and its long-term variation. *Icarus*, *358*, 114172. https://doi.org/10.1016/j.icarus.2020.114172

Goldreich, P. (1966). History of the lunar orbit. *Reviews of Geophysics and Space Physics*, *4*, 411–439. https://doi.org/10.1029/rg004i004p00411

Green, J. A. M., Huber, M., Waltham, D., Buzan, J., & Wells, M. (2017). Explicitly modeled deep-time tidal dissipation and its implication for lunar history. *Earth and Planetary Science Letters*, *461*, 46–53. https://doi.org/10.1016/j.epsl.2016.12.038

Hilgen, F. J., Kuiper, K. F., & Lourens, L. J. (2010). Evaluation of the astronomical timescale for the Paleocene and earliest Eocene. *Earth and Planetary Science Letters*, *300*, 139–151. https://doi.org/10.1016/j.epsl.2010.09.044

Hüsing, S. K., Hilgen, F. J., Abdul Aziz, H., & Krijgsman, W. (2007). Completing the Neogene geological timescale between 8.5 and 12.5 Ma. *Earth and Planetary Science Letters*, *253*(3–4), 340–358. https://doi.org/10.1016/j.epsl.2006.10.036

IPCC. (2013). Intergovernmental Panel on Climate Change. In T. F. Stocker, et al. (Eds.), *Climate Change 2013: The physical science basis* (Vol. 1535). Cambridge: Cambridge University Press.

Kant, I. (1754). Untersuchung der frage, ob die erde in ihrer umdrehung um die achse, wodurch sie die abwechselung des tages und der nacht hervorbringt, einige veränderung seit den ersten zeiten ihres ursprungs erlitten habe und woraus man sich ihrer versichern könne, welche von der königl. akademie der wissenschaften zu berlin zum preise für das jetztlaufende jahr aufgegeben worden. In *Kant's gesammelte schriften* (Vol. 1, pp. 183–191).

Koch, P. L., Zachos, J. C., & Gingerich, P. D. (1992). Correlation between isotope records in marine and continental carbon reservoirs near the Palaeocene/Eocene boundary. *Nature*, *358*, 319–322. https://doi.org/10.1038/358319a0

Kocken, I. J., Cramwinckel, M. J., Zeebe, R. E., Middelburg, J. J., & Sluijs, A. (2019). The 405 Kyr and 2.4 Myr eccentricity components in Cenozoic carbon isotope records. *Climate of the Past*, *15*(1), 91–104. https://doi.org/10.5194/cp-15-91-2019

Kuiper, K. F., Deino, A., Hilgen, F. J., Krijgsman, W., Renne, P. R., & Wijbrans, J. R. (2008). Synchronizing rock clocks of Earth history. *Science*, *320*(5875), 500–504. https://doi.org/10.1126/science.1154339

Kump, L. R., Bralower, T. J., & Ridgwell, A. (2009). Ocean acidification in deep time. *Oceanography*, *22*(4), 94–107. https://doi.org/10.5670/oceanog.2009.100

Lambeck, K. (1980). *The Earth's variable rotation: Geophysical causes and consequences* (p. 449). Cambridge University Press.

Lantink, M. L., Davies, J. H. F. L., Mason, P. R. D., Schaltegger, U., & Hilgen, F. J. (2019). Climate control on banded iron formations linked to orbital eccentricity. *Nature Geoscience*, *12*(5), 369–374. https://doi.org/10.1038/s41561-019-0332-8

Laskar, J., Fienga, A., Gastineau, M., & Manche, H. (2011). La2010: A new orbital solution for the long-term motion of the Earth. *Astronomy & Astrophysics*, *532*, A89. https://doi.org/10.1051/0004-6361/201116836

Laskar, J., Gastineau, M., Delisle, J.-B., Farrés, A., & Fienga, A. (2011). Strong chaos induced by close encounters with Ceres and Vesta. *Astronomy & Astrophysics*, *532*, L4. https://doi.org/10.1051/0004-6361/201117504

Laskar, J., Joutel, F., & Boudin, F. (1993). Orbital, precessional, and insolation quantities from the Earth from −20 Myr to +10 Myr. *Astronomy & Astrophysics*, *270*, 522–533.

Laskar, J., Robutel, P., Joutel, F., Gastineau, M., Correia, A. C. M., & Levrard, B. (2004). A long-term numerical solution for the insolation quantities of the Earth. *Astronomy & Astrophysics*, *428*, 261–285. https://doi.org/10.1051/0004-6361:20041335

Lau, H. C. P., Mitrovica, J. X., Austermann, J., Crawford, O., Al-Attar, D., & Latychev, K. (2016). Inferences of mantle viscosity based on ice age data sets: Radial structure. *Journal of Geophysical Research*, *121*(10), 6991–7012. https://doi.org/10.1002/2016JB013043

Lauretano, V., Littler, K., Polling, M., Zachos, J. C., & Lourens, L. J. (2015). Frequency, magnitude, and character of hyperthermal events at the onset of the Early Eocene Climatic Optimum. *Climate of the Past*, *11*, 1313–1324. https://doi.org/10.5194/cp-11-1313-2015

Lauretano, V., Zachos, J. C., & Lourens, L. J. (2018). Orbitally paced carbon and deep-sea temperature changes at the peak of the Early Eocene Climatic Optimum. *Paleoceanography and Paleoclimatology*, *33*(10), 1050–1065. https://doi.org/10.1029/2018pa003422

Levrard, B., & Laskar, J. (2003). Climate friction and the Earth's obliquity. *Geophysical Journal International*, *154*(3), 970–990. https://doi.org/10.1046/j.1365-246X.2003.02021.x

Li, M., Kump, L. R., Hinnov, L. A., & Mann, M. E. (2018). Tracking variable sedimentation rates and astronomical forcing in Phanerozoic paleoclimate proxy series with evolutionary correlation coefficients and hypothesis testing. *Earth and Planetary Science Letters*, *501*, 165–179. https://doi.org/10.1016/j.epsl.2018.08.041

Lourens, L. J., Antonarakou, A., Hilgen, F. J., Van Hoof, A. A. M., Vergnaud-Grazzini, C., & Zachariasse, W. J. (1996). Evaluation of the Plio-Pleistocene astronomical timescale. *Paleoceanography*, *11*(4), 391–413. https://doi.org/10.1029/96PA01125

Lourens, L. J., Sluijs, A., Kroon, D., Zachos, J. C., Thomas, E., Röhl, U., et al. (2005). Astronomical pacing of late Palaeocene to early Eocene global warming events. *Nature*, *435*, 1083–1087. https://doi.org/10.1038/nature03814

Lourens, L. J., Wehausen, R., & Brumsack, H. J. (2001). Geological constraints on tidal dissipation and dynamical ellipticity of the Earth over the past three million years. *Nature*, *409*(6823), 1029–1033. https://doi.org/10.1038/35059062

Ma, C., & Li, M. (2020). Astronomical timescale of the Turonian constrained by multiple paleoclimate proxies. *Geoscience Frontiers*, *11*(4), 1345–1352. https://doi.org/10.1016/j.gsf.2020.01.013

Meyers, S. R., & Malinverno, A. (2018). Proterozoic Milankovitch cycles and the history of the solar system. *Proceedings of the National Academy of Science*, *115*(25), 6363–6368. https://doi.org/10.1073/pnas.1717689115

Mitrovica, J. X., & Forte, A. M. (2004). A new inference of mantle viscosity based upon joint inversion of convection and glacial isostatic adjustment data. *Earth and Planetary Science Letters*, *225*(1–2), 177–189. https://doi.org/10.1016/j.epsl.2004.06.005

Montenari, M. (Ed.). (2018). *Stratigraphy & timescales: Cyclostratigraphy and astrochronology in 2018* (Vol. 3, p. 384). Elsevier.

Morrow, E., Mitrovica, J. X., Forte, A. M., Glisovic, P., & Huybers, P. (2012). An enigma in estimates of the Earth's dynamic ellipticity. *Geophysical Journal International.*, *191*(3), 1129–1134. https://doi.org/10.1111/j.1365-246X.2012.05703.x

Norris, R. D., Wilson, P. A., Blum, P., Fehr, A., Agnini, C., Bornemann, A., et al. (2014). Paleogene Newfoundland sediment drifts and MDHDS test. In *Proc. IODP* (Vol. 342). College Station, TX: Integrated Ocean Drilling Program.

Pälike, H., & Shackleton, N. J. (2000). Constraints on astronomical parameters from the geological record for the last 25 Myr. *Earth and Planetary Science Letters*, *182*(1), 1–14. https://doi.org/10.1016/s0012-821x(00)00229-6

Quinn, T. R., Tremaine, S., & Duncan, M. (1991). A three million year integration of the Earth's orbit. *The Astronomical Journal*, *101*, 2287–2305. https://doi.org/10.1086/115850

Rauch, K. P., & Hamilton, D. P. (2002). The HNBody package for symplectic integration of nearly-Keplerian systems, in *AAS/Division of Dynamical Astronomy Meeting #33*. *Bulletin of the American Astronomical Society*, *34*, 938.

Ray, R. D., Eanes, R. J., & Lemoine, F. G. (2001). Constraints on energy dissipation in the Earth's body tide from satellite tracking and altimetry. *Geophysical Journal International*, *144*(2), 471–480. https://doi.org/10.1046/j.1365-246X.2001.00356.x

Renne, P. R., Deino, A. L., Hilgen, F. J., Kuiper, K. F., Mark, D. F., Mitchell, W. S., et al. (2013). Timescales of critical events around the Cretaceous-Paleogene boundary. *Science*, *339*(6120), 684–687. https://doi.org/10.1126/science.1230492

Sprain, C. J., Renne, P. R., Clemens, W. A., & Wilson, G. P. (2018). Calibration of chron C29r: New high-precision geochronologic and paleomagnetic constraints from the Hell Creek region, Montana. *Geological Society of America Bulletin*, *130*(9–10), 1615–1644. https://doi.org/10.1130/B31890.1

Stephenson, F. R., Morrison, L. V., & Hohenkerk, C. Y. (2016). Measurement of the Earth's rotation: 720 BCE to CE 2015. *Proceedings of the Royal Society A*, *472*(2196), 20160404. https://doi.org/10.1098/rspa.2016.0404

Stoyko, A. (1970). La variation séculaire de la rotation de la terre et les problémes connexes. *Annales Guebhard*, *6*, 293–316.

Touma, J., & Wisdom, J. (1994). Evolution of the Earth-Moon system. *The Astronomical Journal*, *108*, 1943. https://doi.org/10.1086/117209

Vahlenkamp, M., De Vleeschouwer, D., Batenburg, S. J., Edgar, K. M., Hanson, E., Martinez, M., et al. (2020). A lower to middle Eocene astrochronology for the Mentelle Basin (Australia) and its implications for the geologic timescale, *Earth and Planetary Science Letters*, *529*, 115865. https://doi.org/10.1016/j.epsl.2019.115865

Walker, J. C. G., & Zahnle, K. J. (1986). Lunar nodal tide and distance to the Moon during the Precambrian. *Nature*, *320*(6063), 600–602. https://doi.org/10.1038/320600a0

Ward, W. R. (1974). Climatic variations on Mars: 1. Astronomical theory of insolation. *Journal of Geophysical Research*, *79*(24), 3375–3386. https://doi.org/10.1029/JC079i024p03375

Ward, W. R. (1979). Present obliquity oscillations of Mars: Fourth-order accuracy in orbital *e* and *I*. *Journal of Geophysical Research*, *84*, 237–241. https://doi.org/10.1029/jb084ib01p00237

Westerhold, T., Röhl, U., Bohaty, S., Florindo, F., Frederichs, T., Zachos, J., & Agnini, C. (2019). Revision of the middle Eocene astronomical timescale—New high-resolution stable isotope records between 38 and 49 Ma. In *EGU General Assembly Conference Abstracts, 2019* (Vol. 12, p. 894).

Williams, G. E. (2000). Geological constraints on the Precambrian history of Earth's rotation and the Moon's orbit. *Reviews of Geophysics*, *38*(1), 37–59. https://doi.org/10.1029/1999RG900016

Wisdom, J., & Holman, M. (1991). Symplectic maps for the n-body problem. *The Astronomical Journal*, *102*, 1528–1538. https://doi.org/10.1086/115978

Zachos, J. C., Pagani, M., Sloan, L., Thomas, E., & Billups, K. (2001). Trends, rhythms, and aberrations in global climate 65 Ma to present. *Science*, *292*, 686–693. https://doi.org/10.1126/science.1059412

Zachos, J. C., Röhl, U., Schellenberg, S. A., Sluijs, A., Hodell, D. A., Kelly, D. C., et al. (2005). Rapid acidification of the ocean during the Paleocene-Eocene thermal maximum. *Science*, *308*, 1611–1615. https://doi.org/10.1126/science.1109004

Zeebe, R. E. (2015a). Dynamic stability of the solar system: Statistically inconclusive results from ensemble integrations. *The Astrophysical Journal*, *798*, 8. https://doi.org/10.1088/0004-637X/798/1/8

Zeebe, R. E. (2015b). Highly stable evolution of Earth's future orbit despite chaotic behavior of the solar system. *The Astrophysical Journal*, *811*, 9. https://doi.org/10.1088/0004-637X/811/1/9

Zeebe, R. E. (2017). Numerical solutions for the orbital motion of the solar system over the past 100 Myr: Limits and new results. *The Astronomical Journal*, *154*, 193. https://doi.org/10.3847/1538-3881/aa8cce

Zeebe, R. E., & Lourens, L. J. (2019). Solar system chaos and the Paleocene-Eocene boundary age constrained by geology and astronomy. *Science*, *365*, 926–929. https://doi.org/10.1126/science.aax0612

Zeebe, R. E., Ridgwell, A., & Zachos, J. Z. (2016). Anthropogenic carbon release rate unprecedented during past 66 Myr. *Nature Geoscience*, *9*, 325–329. https://doi.org/10.1038/ngeo2681

Zeebe, R. E., Westerhold, T., Littler, K., & Zachos, J. C. (2017). Orbital forcing of the Paleocene and Eocene carbon cycle. *Paleoceanography*, *32*(1), 440–465. https://doi.org/10.1002/2016PA003054

Zeebe, R. E., Zachos, J. C., & Dickens, G. R. (2009). Carbon dioxide forcing alone insufficient to explain Palaeocene-Eocene Thermal Maximum warming. *Nature Geoscience*, *2*, 576–580. https://doi.org/10.1038/ngeo578

Zeeden, C., Hilgen, F. J., Hüsing, S. K., & Lourens, L. L. (2014). The Miocene astronomical timescale 9–12 Ma: New constraints on tidal dissipation and their implications for paleoclimatic investigations. *Paleoceanography*, *29*(4), 296–307. https://doi.org/10.1002/2014PA002615

Zeeden, C., Hilgen, F., Westerhold, T., Lourens, L., Röhl, U., & Bickert, T. (2013). Revised Miocene splice, astronomical tuning and calcareous plankton biochronology of ODP Site 926 between 5 and 14.4 Ma. *Paleogeography, Paleoclimatology, Paleoecology*, *369*, 430–451. https://doi.org/10.1016/j.palaeo.2012.11.009